Thermodynamic pathway for the formation of SnSe and $SnSe_2$ polycrystalline thin films by selenization of metal precursors

P. A. Fernandes,[ab†] M. G. Sousa,[a] P. M. P. Salomé,[c] J. P. Leitão[a] and A. F. da Cunha[a]

Received Xth XXXXXXXXXX 20XX, Accepted Xth XXXXXXXXX 20XX
First published on the web Xth XXXXXXXXXX 200X
DOI: 10.1039/b000000x

In this work, tin selenide thin films ($SnSe_x$) were grown on soda lime glass substrates by selenization of dc magnetron sputtered Sn metallic precursors. Selenization was performed at maximum temperatures in the range of 300 °C to 570 °C. The thickness and the composition of the films were analysed using step profilometry and energy dispersive spectroscopy, respectively. The films were structurally and optically investigated by X-Ray diffraction, Raman spectroscopy and optical transmittance and reflectance measurements. X-Ray diffraction patterns suggest that for temperatures between 300 °C and 470 °C the films are composed of hexagonal-$SnSe_2$ phase. By increasing the temperature, the films selenized at maximum temperatures of 530 °C and 570 °C show orthorhombic-SnSe as the dominant phase with a preferential crystal orientation along the (400) crystallographic plane. Raman scattering analysis allowed the assignment of peaks at 119 cm^{-1} and 185 cm^{-1} to the hexagonal-$SnSe_2$ and 108 cm^{-1}, 130 cm^{-1} and 150 cm^{-1} to the orthorhombic-SnSe phase. All samples present traces of condensed amorphous Se with a characteristic Raman peak located at 255 cm^{-1}. From optical measurements, the estimated band gap energies for hexagonal-$SnSe_2$ were close to 0.9 eV and 1.7 eV for indirect forbidden and direct transitions, respectively. The samples with the dominant orthorhombic-SnSe phase presented estimated band gap energies of 0.95 eV and 1.15 eV for indirect allowed and direct allowed transitions, respectively.

1 Introduction

Thin films of metal chalcogenides have attracted considerable attention due to theirs application prospects, in infrared optoelectronic devices, radiation detectors, memory devices and holographic recording systems [1–6]. In particular, binary compounds such as tin monoselenide, SnSe, and tin diselenide, $SnSe_2$, are seen by the community as potential candidates for photovoltaic applications [7].

Tin monoselenide is a p-type semiconductor with a band gap close to 0.9 eV for indirect allowed transitions [8–10] and 1.2 eV for direct allowed transitions [8,10–15]. SnSe melts congruently at 880 °C. There are two known polymorphous crystalline structures. At 535 °C, the low temperature α-phase corresponding to an orthorhombic structure transforms into high temperature β-phase corresponding to an cubic structure. The SnSe phase transitions are of second order and extend up to 200 °C [16].

[a] *I3N and Departamento de Física, Universidade de Aveiro, Campus Universitário de Santiago, 3810-193 Aveiro, Portugal. Fax: +351 234 378 197; Tel: +351 234 370 356;*
[b] *Departamento de Física, Instituto Superior de Engenharia do Porto, Instituto Politécnico do Porto, Rua Dr. António Bernardino de Almeida, 431, 4200-072 Porto, Portugal;*
[c] *Ångström Solar Center, Solid State Electronics, Uppsala University, Ångström Laboratory PO Box 534, SE-751 21 Uppsala, Sweden;*
† *Corresponding author; E-mail: pafernandes@ua.pt.*

Tin diselenide is a n-type semiconductor and the values for the band gap energies found most frequently in the literature are close to 0.95 eV for indirect forbidden transitions [17–19]. Au-Yang *et al.* predicted slightly lower values, 0.81 eV, for the same kind of transition using the empirical pseudopotential method [20]. Indirect allowed transitions were also observed by Pramanik *et al.* with bang gap energies close to 0.95 eV [21]. Direct allowed and forbidden transitions were also estimated with band gap energies of 2.1 eV [18,19] and 1.62-1.78 eV [17,20], respectively. Recently, Martínez-Escobar *et al.* estimated an optical band gap of 1.59 eV for direct allowed transitions [22]. Tin diselenide is a group-IV dichalcogenide and presents a hexagonal crystallographic structure CdI_2-type (C6). It is formed by strongly bonded (mainly covalent bonds) two-dimensional Se-Sn-Se layers. In contrast, these layers are weakly coupled along the c axis by van der Waals forces. This property enables the formation of 10 polytypes [23] by lattice relaxations for the repetition unit along the stacking axis [24]. According to Palosz *et al.* the most common polytypes are 2H and 18R [24].

A wide variety of synthesis methods have been reported for the growth of tin selenide and tin diselenide. Atmospheric pressure processes such as chemical bath deposition and solvothermal routes [21,25–27], electrodeposition and brush plating [7,9,14,28], and spray pyrolysis [22] have been used to grow SnSe thin films. Boscher *et al.* [29] developed a method based on

chemical vapor deposition. Vacuum environment techniques such as flash, conventional and reactive evaporation[8,10,12,13], hot wall epitaxy[11], atomic layer deposition[30] and pulsed laser deposition[31,32] can also be found in literature. For $SnSe_2$ thin films synthesis, Hady *et al.*[33] successfully tested conventional thermal evaporation of Sn and Se, and $SnSe_2$ powders. Bulk precursors were also used to deposit thin film layers by the same technique[19]. Reports on the growth of layered $SnSe_2$ films on a variety of layered substrates using van der Waals epitaxy can be found on literature[34]. Other methods showed to be able to synthesize $SnSe_2$ thin layers such as spray pyrolysis[22,35], pulsed laser deposition[36] and chemical vapor deposition[29].

In this work we propose a method to grow SnSe or $SnSe_2$ thin films based on the deposition of tin metallic precursors by DC-magnetron sputtering followed by an annealing step in a Se vapour atmosphere. We report the effect of the annealing temperature on the properties of the films. The crystalline structure of the films has been studied by X-ray diffraction and Raman scattering spectroscopy. The characterization of the morphology is done by scanning electron microscopy. The spectrophotometry measurements allowed the study of the optical behaviour of the samples and the determination of the band gap energies of the compounds.

2 Sample characterization

The thickness of the individual metallic precursors and the final selenized layer thicknesses were measured using a Dektak 150 step profiler. The crystalline structure was studied by X-Ray Diffraction (XRD) with XPert MPD Philips diffractometer, in the Bragg-Brentano configuration (θ-2θ), using the Cu-Kα line (λ =1.540598 Å) and the generator settings were 50 mA and 40 kV. A LabRam Horiba HR800 UV spectrometer, equipped with an Olympus microscope with a 100 magnification lens, was used for the Raman scattering measurements. This equipment uses the backscattering configuration. The samples were analysed using two excitation laser lines, 325 nm and 532 nm. The optical arrangement allowed to focus the laser beam down to a spot size of 1 μm in diameter. This equipment had a resolution of 1 cm^{-1}. With the aim of avoiding damage in the samples, the power of the laser beam was reduced to values below 0.5 mW using attenuating filters. Optical measurements were done using a Shimadzu UV3600 spectrophotometer equipped with an integrating sphere. The surface morphology and compositional analysis of the resulting films were performed by scanning electron microscopy (SEM) and energy dispersive spectrometry (EDS). The system was a SU-70 Hitachi with a Rontec EDS system and the acceleration voltages used were 25 kV and 4 kV for composition and morphology analysis, respectively. The sample naming scheme uses the selenium element symbol Se followed by the maximum selenization temperature.

3 Sample preparation

The growth method used in this work is constituted by two stages. The first one refers to the deposition of the metallic precursor layer, Sn, by DC magnetron sputtering. The chalcogen incorporation, Se, and the annealing process, which allow the crystalline phase formation, are performed in the second stage. The sample preparation process begins with the cleaning of 3 by 3 cm soda lime glass (SLG) substrate, with successive ultrasound baths of acetone/alcohol/deionised water. This step ends with the substrate being dried with a N_2 flow. Next, the precursor layer was deposited directly on the SLG using an Ar atmosphere at an operating pressure of 2×10^{-3} mbar. The target purity was 99.99%. To avoid the target's melting, a low energy density of 0.11 Wcm^2 was used. *In situ* monitoring of the layer thicknesses was done with a quartz crystal monitor. For the second stage, a temperature controlled tubular furnace was used. The samples were placed inside a graphite box together with 240 mg of high purity Se pellets and heated in a N_2+ 5% H_2 atmosphere at an operating pressure of 600 mbar. The programmed sample heating rate was set to be 10 K/min. The selenization temperature profiles are shown in Figure 1. In this stage, the parameter that changed between samples was the maximum selenization temperature, which ranged from 300 °C to 570 °C.

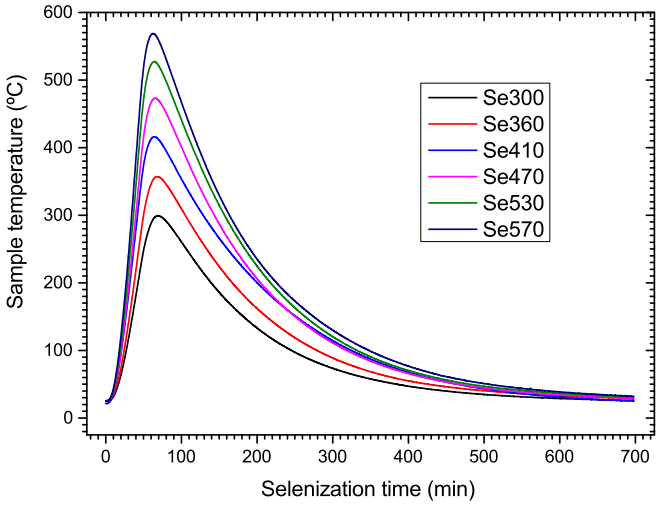

Fig. 1 Selenization temperature profiles for the studied samples.

4 Results and discussion

4.1 Composition results

The Figure 2 shows the EDS spectra of the studied samples. These results show prominent peaks at 1.39 keV and 3.44 keV which correspond to the sum of the Se-L_{α} and Se-$L_{\beta 1}$, and Sn-L_{α} X-ray emission lines, respectively. Less intense characteristic peaks attributed to Sn are also observed at 3.68 keV, 3.91 keV and 4.11 keV assigned to Sn-$L_{\beta 1}$, Sn-$L_{\beta 2}$ and Sn-$L_{\gamma 1}$ emission lines, respectively. Comparing the intensities of the Se-L_{series} and the Sn-L_{series} emission lines for the samples with increasing selenization temperatures, it can be observed a significant decrease of the Se signal counts. EDS quantification models allowed to determine that the samples selenized at higher temperatures, namely Se530 and Se570, are Se-poorer than the samples annealed at lower temperatures. Additional contributions to the EDS spectra such as the Ca-L_{α} (0.34 keV), Ca-K_{α} (3.68 keV), Ca-$K_{\beta 1}$ (3.95 keV), Na-K_{α} (1.04 keV), Mg-K_{α} (1.24 keV) and Si-K_{α} (1.74 keV) emission lines can also be observed . These emissions are mainly from elements that constitute the substrate. Nevertheless, it is known that some elements such Na and K easily diffuse to the film under high temperature annealing processes. The C-$K_{\alpha 1}$ emission line with an energy of 0.28 keV result from the sample preparation process.

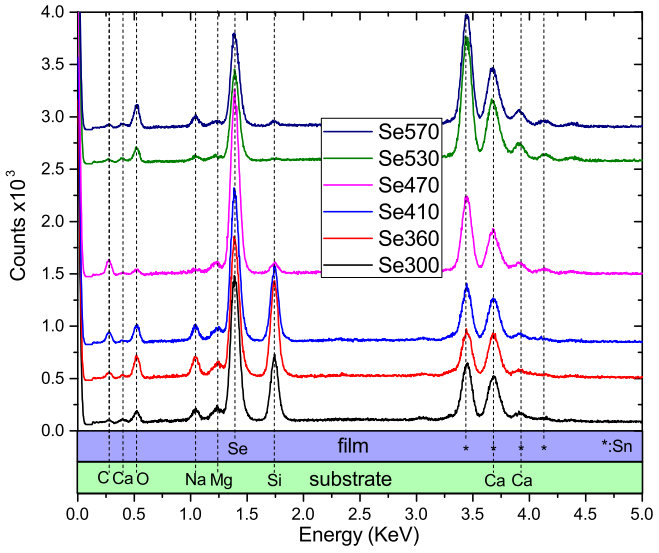

Fig. 2 EDS analysis spectra for the studied samples. Peak assignments of the elements according X-Ray Data Booklet[37].

Table 1 shows the composition ratios, $\frac{[Se]}{[Sn]}$, based on the results discussed previously. For the samples selenized at lower temperatures, the ratios are close to 2.0 which is the value for stoichiometric $SnSe_2$. As mentioned before, for Se530 and Se570, the Se content decreases to values equal to 0.91. Within measurement uncertainties, these compositions approach the value 1.0, which is the ratio for stoichiometric SnSe.

Table 1 Se and Sn composition ratio for the studied samples. Data obtained *via* EDS analysis.

Sample	Ratio $\frac{[Se]}{[Sn]}$
Se300	1.94
Se360	2.19
Se410	2.16
Se470	1.94
Se530	0.91
Se570	0.91

4.2 Thickness evaluation

Table 2 shows the results of the thickness measurements of the selenized layers. As shown in this table, all precursor layers had a thickness of 450 nm. It is also included the estimation of the relative thickness variation of the films after the selenization process. The results show a clear decrease of the thicknesses with the increase of the selenization temperature.

Table 2 Thicknesses of the metallic precursors and selenized films measured by step profiler. Relative thickness variation for the selenized samples compared with the precursors layers.

Sample	Thickness (nm)	Relative thickness variation (%)
Precursor	450	-
Se300	1033	130
Se360	992	120
Se410	973	116
Se470	949	111
Se530	766	70
Se570	747	66

A more detailed analysis of this behaviour is presented in Figure 3. For the temperature range from 300 °C to 470 °C, the thickness decreases at an average slope of 0.49 nm/°C. A similar slope, 0.48 nm/°C, is observed for the temperature range of 530 °C to 570 °C. A greater slope was expected for higher temperatures, because the samples were exposed to an higher temperature for a longer time. These losses were mainly attributed to material sublimation. This loss mechanism seems not to be enough to explain a negative slope of 3.05 nm/°C between selenization temperatures of 470 °C and 530 °C. As it will be shown in the following sections, this temperature interval seems to define the thermodynamic conditions to the formation of a different phase, namely SnSe. This phase present different properties from the one formed at lower selenization temperatures, $SnSe_2$. This fact may explain the additional thickness decrease observed in Figure 3.

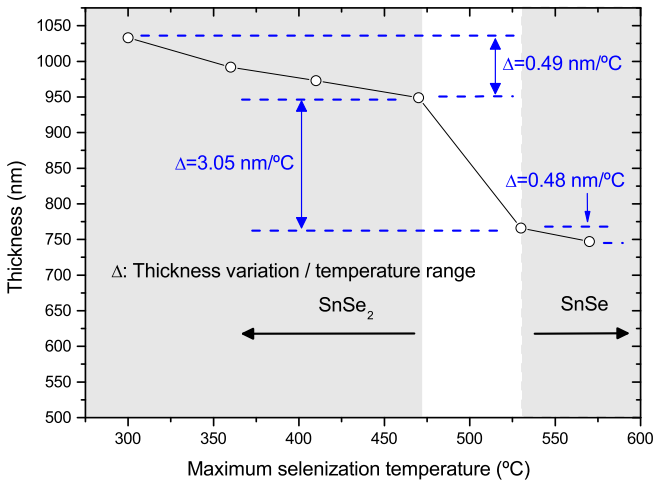

Fig. 3 Layer thickness *vs.* maximum selenization temperature for the studied samples.

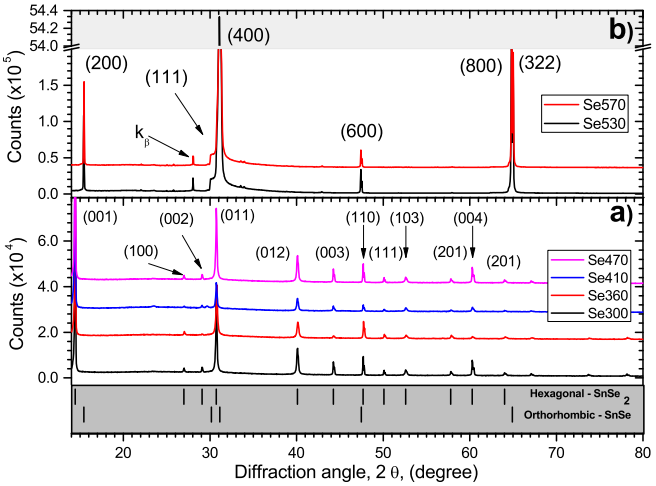

Fig. 4 XRD diffractograms for the five selenized samples with maximum temperatures ranging 300 °C to 470 °C (a) and 530 °C to 570 °C (b). The phase assignment was done using the ICDD database[38].

4.3 Structural study

The structural analysis was preformed using XRD and Raman scattering techniques. Figure 4 shows the results of XRD measurements for the five tested maximum selenization temperatures. The assignment of the phases was done using the International Centre for Diffraction Data (ICDD) database[38]. Figure 4 a) shows that for selenization temperatures ranging from 300 °C to 470 °C, the dominant phase is $SnSe_2$ with a hexagonal structure (space group P-3m1 (164))[38]. From this diffraction pattern it can be seen that the peaks are sharp which suggests that the samples have good crystalline quality. The diffractograms also present the highest counts for the peak located at a diffraction angle, 2θ , 14.44°, which correspond to the (0 0 1) planes. The formation of this phase from metallic Sn precursors and Se vapour may be interpreted as the result of the association reaction defined as follows:

$$\mathrm{Sn(s)} + 2\,\mathrm{Se(g)} \longrightarrow \mathrm{SnSe_2(s)} \qquad (1)$$

as suggested by Melekh *et al.*[39] for a Se rich atmosphere ([Se]≥ 67%). Considering the selenization conditions for the lower temperature range, it is expected that the most abundant Se species are Se_8 and to a lesser extend Se_7 and Se_6. Increasing the temperature, the dominant Se specie becomes Se_2[40]. The presence of H_2 in the selenization atmosphere can play a major role in formation reaction 1, promoting de formation of H_2Se which in turn provides atomic Se for the formation of $SnSe_2$.

As shown in Figure 4 b), the samples selenized at maximum temperature of 530 °C and 570 °C suggest the presence of a different phase, namely α-SnSe with a orthorhombic structure (space group Pbnm (62))[38]. These diffractograms show that the most important peak is located at 31.15° for the (4 0 0) planes. The formation of this phase may rely on the Se atmosphere depletion in a later stage of the selenization process. This is due to high selenization temperatures during extended time intervals considering the same starting chalcogen amount. Therefore, it is expected that in the Se530 and Se570 growth, two intermediate processes could be involved in the synthesis of SnSe. Initially, in the high Se availability regime, the $SnSe_2$ formation occurs according to reaction 1. After that, Se depletion and high temperatures promote dissociation processes. The chalcogen depletion occurs mainly by localized film segregation and by condensation in other parts of the furnace and exhaustion system. Two different routes for this dissociation reaction are proposed in literature. One is based on the complete dissociation reaction[39,41]:

$$\mathrm{SnSe_2(s)} \longrightarrow \mathrm{Sn(s)} + 2\,\mathrm{Se(g)} \qquad (2)$$

followed by, in the final step, when a Se poor atmosphere ([Se]<67 %) is present, by the formation of SnSe through the reaction[39,42]:

$$\mathrm{Sn(s)} + \mathrm{Se(g)} \longrightarrow \mathrm{SnSe(s)} \qquad (3)$$

The alternative route is based on the incongruent sublimation of the $SnSe_2$ and proposes the direct formation of the SnSe from $SnSe_2$ through the reaction[43]:

$$\mathrm{SnSe_2(s)} \longrightarrow \mathrm{SnSe(s)} + \frac{1}{x}Se_x\mathrm{(g)} \qquad (4)$$

where $x = 2-8$, which represent the various Se species that can be formed during this process. In both cases, the final

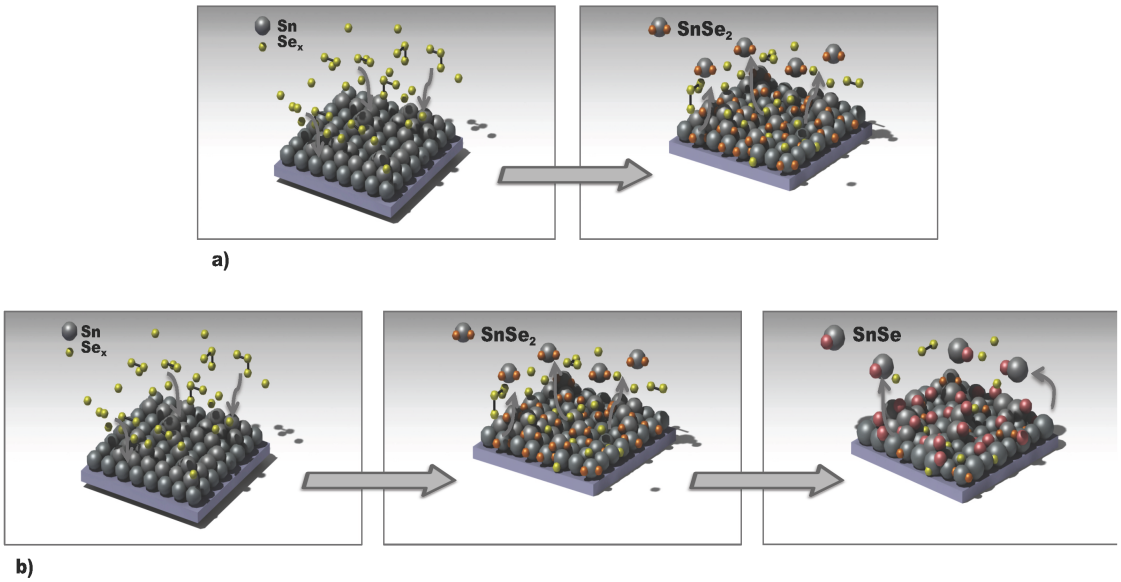

Fig. 5 Reaction schematics of the SnSe and $SnSe_2$ growth for a) low selenization temperature profiles (300 °C $\mapsto$ 470 °C) and for b) high selenization temperature profiles (530 °C $\mapsto$ 570 °C).

results are in accordance with the P-T phase diagram for the Sn-Se system, presented by R. C. Sharma and Y. A. Chang[44], despite being done at higher selenization pressures. For samples selenized at higher temperatures, Se530 and especially Se570, one would expect the formation of the β-SnSe phase. However, this was not confirmed by any of the techniques used in this work. Differences in the growth conditions may cause the α- to β- transition to shift to higher temperatures.

Figure 5 shows a simplified scheme of the reactions involved a) in the formation of the $SnSe_2$ for the low selenization temperature profiles, corresponding to samples Se300 to Se470, and b) in the formation of SnSe for the high selenization temperature profiles, corresponding to samples Se530 and Se570.

Next, the quantitative estimation of the the preferred structural orientation in the $< 00l >$ planes for the set of samples selenized at lower temperatures and in the $< h00 >$ planes for the remaining samples is presented. The degree of orientation, was calculated using the Lotgering method[45]. This procedure defines, F, also known as Lotgering factor, by the following expression:

$$F^{<00l>} = \frac{\frac{\sum I_{\{00l\}}}{\sum I_{\{hkl\}}} - \frac{\sum I_{0\{00l\}}}{\sum I_{0\{hkl\}}}}{1 - \frac{\sum I_{0\{00l\}}}{\sum I_{0\{hkl\}}}}, \quad (5)$$

where I and I_0 are the peak intensities of the textured and randomly oriented phase, respectively. The data for the latter was extracted from standard powder datasheets[38]. Diffraction peaks in the 2θ range from 14° to 80°, as shown in Figure 4, were used for the calculations. As shown in Figure 6, the Lotgering factors for samples selenized at lower temperatures, from 300 °C to 470 °C, point to a slight increase from $\simeq 0.55$ to $\simeq 0.65$. These values suggest a moderate texturization of the samples. This figure also presents the full width at half maximum (FWHM) value of the main peak of the diffraction pattern for each sample. These peaks were located at 2θ, 14.43°, corresponding to the orientation plane (0 0 1). It can be observed that this parameters decreases sharply for the same range of temperatures, from 0.28° to 0.15°. The relation between the latter and crystallite size allow us to conclude that the crystallinity of the samples increases significantly with increasing selenization temperature. For higher temperatures, the Lotgering factors reach values close to 1.0 with no significant variation between them. This means that the samples are formed by almost fully oriented crystallites. For these samples, the measured FWHM of the main peaks located at 2θ, 31.15°, corresponding to the (4 0 0) planes, reaches values close to 0.12°, which suggest a high degree of crystallinity.

4.4 Raman scattering results

Figure 7 shows the Raman scattering results of the studied samples. The spectra shown in Figure 7 refer to results using a laser excitation wavelength of 532 nm and the inset shows the spectra obtained for the lowest and highest selenization temperatures with a laser excitation wavelength of 325 nm. For

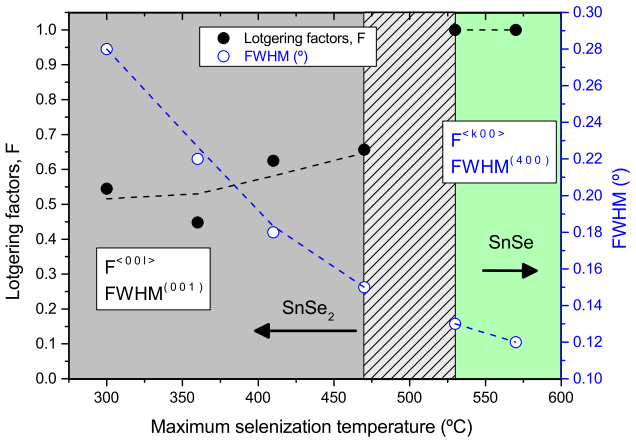

Fig. 6 Closed circles, •, Lotgering factors, $F^{<00l>}$ and $F^{<h00>}$ for samples from Se300 to Se470 and for Se530 and Se570, respectively. Open circles, ○, $FWHM^{(001)}$ and $FWHM^{(400)}$ for the same sample groups.

selenization temperatures from 300 °C to 470 °C, two main peaks located at 119 cm^{-1} and 185 cm^{-1} are seen, which according to Pérez-Vicente *et al.*[46] are characteristic of the $SnSe_2$ phase. The first peak refers to the E_g mode and the second one to the A_{g1} mode. Broad peaks located at 255 cm^{-1} suggest the presence of amorphous Se, a-Se[47]. This peak is present in all samples and it can be due to condensation during the selenization process, most likely from the cooling period. For samples selenized at a maximum temperature of 530 °C and 570 °C, the Raman spectra show three peaks located at 108 cm^{-1}, corresponding the vibration mode B_{3g}, 130 cm^{-1} and 150 cm^{-1}, both related to A_g vibration mode. These peaks correspond to the SnSe phase[48]. Due to the presence of the minor peaks located at 185 cm^{-1}, these results suggest the presence of a residual amount of $SnSe_2$. The XRD technique was unable to detect this phase in these samples, mainly due to the fact that it is a bulk method and therefore hiding the residual phase signal below the noise threshold. Raman scattering also allows a more localized analysis of the sample. In some samples, namely Se410 and Se530, a small shoulder can be observed close to 235 cm^{-1}. This feature corresponds to Se with a trigonal structure which remains on the surface after the growth process[47].

In addition to phase identification, Raman analysis can also provide useful information about spacial location of the phases[49]. As shown in Figure 7, comparing the Raman spectra from visible and UV radiation, it is clear that the peaks referring to $SnSe_2$, located at 180 cm^{-1}, are the most prominent for UV radiation analysis. Only a small shoulder located at 150 cm^{-1} and assigned to SnSe is visible for Se570. This result suggest that SnSe is located deeper in the layer for sample Se570. This assumption is based in the fact that UV radiation penetrates less than 100 nm in high optical absorption materials[50], limiting the Raman scattering analysis to the surface region.

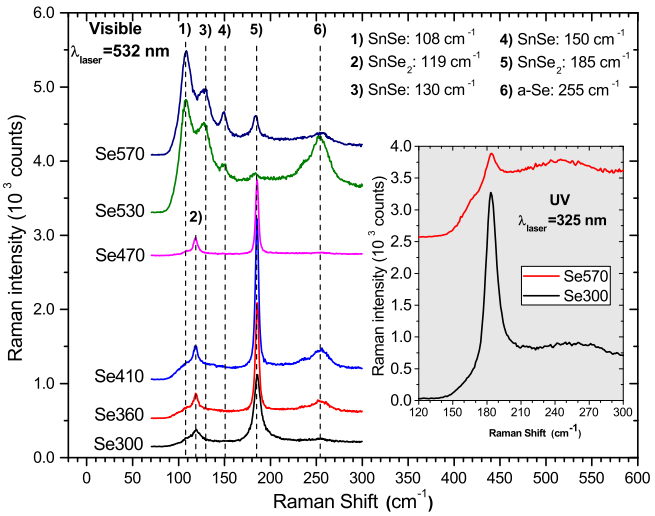

Fig. 7 Raman scattering results of the studied samples for the 532 nm laser excitation wavelength. Peak assignment for SnSe, $SnSe_2$, a-Se are according to literature[46–48]. Inset graph shows the Raman scattering spectra for samples Se300 and Se570 using the 325 nm laser excitation wavelength.

4.5 Optical analysis and band gap determination

The results of the optical reflectance, R, and transmittance, T, measurements are shown in Figure 8 a) and b), respectively. These graphs show that for the samples selenized at higher temperature, 530 °C and 570 °C, the reflectance has little spectral dependence, presenting a maximum of 20 %, close to 700 nm. For lower selenization temperatures, the samples show a reflectivity edge at wavelengths close to 1000 nm. This edge seems to be slightly shifted to higher wavelengths for the sample Se470. The transmittance results show a clear step between two optical regimes for the samples selenized at lower temperatures. This step seems to be located close to 1000 nm. Again, for sample Se470 this transition seems to occur at higher wavelengths, ≅ 1100 nm. Despite having an evident decrease from the IR to the visible region, the samples Se530 and Se570, do not present a well defined transmittance edge as shown for the samples selenized at lower temperatures. The Figure 8 c) presents the optical absorption coefficient, α, plotted against the radiation wavelength for all studied samples as obtained from equation:[51]

$$\alpha = \frac{1}{t}\ln\left[\frac{(1-R)^2+\sqrt{(1-R)^4+(2RT)^2}}{2T}\right] \qquad (6)$$

where for the thicknesses of the layers, t, the values shown in table 2 were used. As shown in figure 8 c), all samples have high optical absorption coefficients, above 10^4 cm^{-1}, which makes them suitable for application as thin film solar cell optical absorbers. The absorption threshold for samples selenized at higher temperatures, Se530 and Se570, seems to be located at slightly lower energies than the ones selenized at lower temperatures.

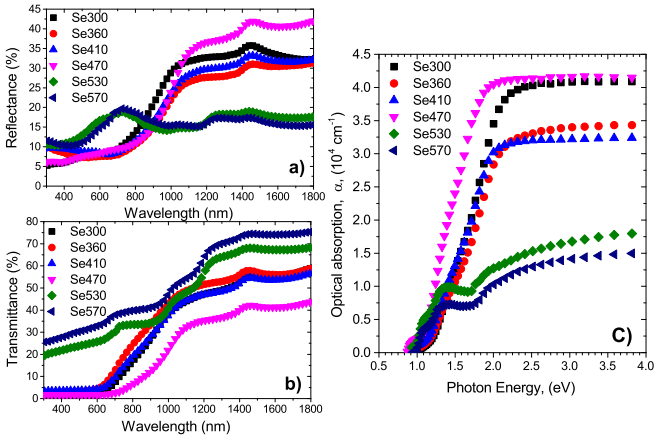

Fig. 8 a) Reflectance measurement results for the studied samples plotted against the radiation wavelength from 300 nm to 1800 nm, b) Transmittance measurement results for the studied samples plotted against the radiation wavelength from 300 nm to 1800 nm, c) Optical absorption coefficient for studied samples against the photon energy.

As stated by Bardeen *et al.*[52] and Smith[53], the relation between the absorption coefficient and the nature of the optical transition can be defined by the following expression:

$$(\alpha h\nu)^m = A(h\nu - E_g) \tag{7}$$

where A is a constant, m defines the nature of the transition, $h\nu$ is the photon energy and E_g is the band gap energy. The value of the power m is $1/2$ (allowed) or $1/3$ (forbidden) for indirect transitions and 2 (allowed) or $2/3$ (forbidden) for direct transitions. To estimate which types of transitions generate the absorption edges shown in figure 8 c), the values of $(\alpha h\nu)^m$ were plotted against the photon energy. As shown in Figure 9, the band gap energy estimation was divided into two groups. Figure 9 a) refers to lower selenization temperatures samples, Se300 to Se470, where $SnSe_2$ was found to be the dominant phase. In the region 0.8-1.4 eV, indirect transitions were expected. From the two powers previously mentioned the best results were obtained for $m = 1/3$, which means that the nature of the transition was indirect forbidden. As presented in Figure 9 a), extrapolating the results of $(\alpha h\nu)^{1/3}$ to zero the band gap energies point to values close to 0.90 eV. These values are in good agreement with previously reported values[17,19,20]. At a photon energy above 1.4 eV, where optical absorption coefficients are high, the calculations show that the best results were found when $m = 2$. This indicates a direct allowed transition. Extrapolations of the straight lines gave values of allowed direct energy gap between 1.62-1.69 eV for the samples selenized at 300 °C, 360 °C and 410 °C. These values were lower than the value published for the same transition type, which were close to 2.0 eV[19,54]. Some authors also reported forbidden direct transitions for this phase, with values between 1.62 eV and 1.78 eV[17,20]. Attempts to fit the data to the corresponding power values revealed unrealistic narrow bands. In the case of sample Se470, the band gap value was lower, 1.43 eV, which despite the fact that it was not detected with other techniques, may be related with the presence of SnSe phase in the sample. For samples Se530 and Se570, shown in Figure 9 b), the same procedure was applied to the region 0.9-1.1 eV and it points to indirect allowed transitions with band gap energies of 0.94 and 0.96 eV. Similar results were obtained for samples obtained with different growth methods[8,15]. For higher photon energies, the best linear fittings were obtained for direct allowed transitions. The energy values for both samples were 1.15 eV. These results are slightly lower than the values presented in the literature for this type of transition[8,10–12,15]. The reported forbidden direct transition types[7], were not confirmed in this work.

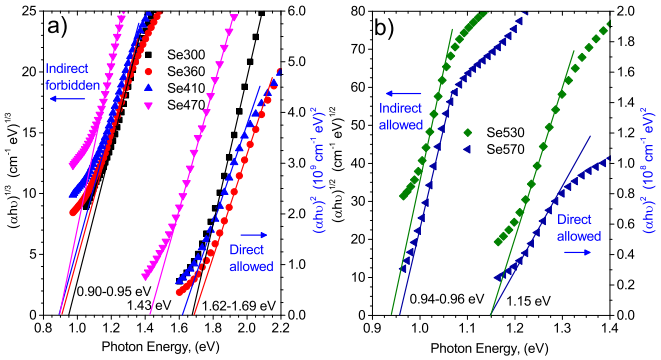

Fig. 9 Band gap energy estimation for the samples a) Se300, Se360, Se410 and Se470 b) Se530 and Se570.

4.6 Morphological analysis

The surface morphology was performed by SEM imaging. Figure 10 shows the results of this analysis for all the studied samples. Based on the morphology, the results were divided in three groups. The first one refers to the samples selenized at 300 °C and 360 °C. SEM micrographs show a morphology characterized by small surface grains. A slight improvement in the surface regularity with the increase of the selenization temperature can be observed when compar-

ing Se360 with Se300. The second group is formed by samples Se410 and Se470. SEM analysis reveal disk-like grains morphologies (more evident in sample Se470). This feature is well explained by the layered structure mentioned in section 1, for the $SnSe_2$ compound. Similar morphology can be found in literature[29,55]. The last group refers to samples consisting mainly in SnSe. These samples present a regular morphology formed by large grains (in some cases with lateral dimensions greater than 10 μm). Some cracks are also observed that may be due film tension.

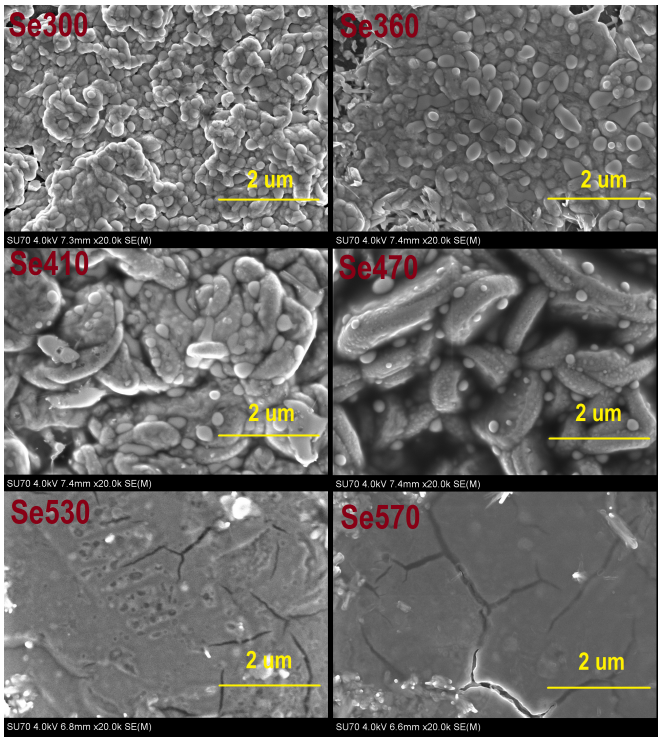

Fig. 10 Surface SEM micrographs of the studied samples.

5 Conclusions

In this work, it is shown that the two step method can be used to grow $SnSe_2$ and SnSe films. This method is based on the deposition of a tin metallic layer and a post annealing process in a selenium atmosphere. Low selenization temperatures, ranging from 300 °C to 470 °C, leads to films where the $SnSe_2$ phase is dominant while selenization at high temperatures, ranging from 530 °C to 570 °C, leads to films where SnSe is the dominant phase. Furthermore, selenization at high temperatures leads to highly textured SnSe films. The optical analysis allowed the estimation of the band gap energies. For the $SnSe_2$ phase the values were $\simeq$ 0.90 eV and $\simeq$ 1.7 eV, for indirect forbidden and direct allowed transitions, respectively. The SnSe showed band gap energies of $\simeq$ 0.95 eV and $\simeq$ 1.15 eV for indirect allowed and direct allowed transitions, respectively. The morphological analysis confirms the $SnSe_2$ disk-like grain morphology. The SnSe films are formed by compact, regular and large grains. Further tests and improvements should be implemented, namely to pin point the optimum selenization pressure, to reduce the formation of secondary phases to undetectable amounts.

6 Acknowledgements

This work is supported by the projects PTDC/CTM-MET/113486/2009 and PEst-C/CTM/LA0025/2011 funded by Fundação para a Ciência e Tecnologia (FCT). FCT is also acknowledged for the financial support of the national electronic microscopy network, whose services we have used, through the Grant REDE/1509/RME/2005.

References

1 T. C. Harman and I. Melngailis, *Applied Solid State Science*, Academic Press, New York, R. Wolfe edn, 1974.
2 L. Wang, B. Niu, Y. T. Lee, D. A. Shirley and K. Balasubramanian, *J. Chem. Phys.*, 1990, **92**, 899–908.
3 C. R. Baxter and W. D. Mclennan, *J. Vac. Sci. Technol.*, 1975, **12**, 110–113.
4 D. Chun, R. M. Walser, R. W. Ben and T. H. Courtney, *Appl. Phys. Lett.*, 1974, **24**, 479–481.
5 K.-M. Chung, D. Wamwangi, M. Woda, M. Wuttig and W. Bensch, *J. Appl. Phys.*, 2008, **103**, 083523.
6 G. Valiukonis, D. A. Guseinova, G. Keivaitb and A. Sileika, *phys. status solidi (b)*, 1986, **135**, 299–307.
7 N. Mathews, *Sol. Energy*, 2012, **86**, 1010–1016.
8 H. S. Soliman, D. A. A. Hady, K. F. A. Rahman, S. B. Youssef and A. A. El-Shazly, *Physica A*, 1995, **216**, 77–84.
9 B. Subramanian, T. Mahalingam, C. Sanjeeviraja, M. Jayachandran and M. J. Chockalingam, *Thin Solid Films*, 1999, **357**, 119–124.
10 G. H. Chandra, J. N. Kumar, N. M. Rao and S. Uthanna, *J. Cryst. Growth*, 2007, **306**, 68–74.
11 J. P. Singh and R. K. Bedi, *J. Appl. Phys.*, 1990, **68**, 2776–2779.
12 K. J. John, B. Pradeep and E. Mathai, *J. Mater. Sci.*, 1994, **29**, 1581–1583.
13 D. P. Padiyan, A. Marikani and K. R. Murali, *Cryst. Res. Technol.*, 2000, **35**, 949–957.
14 Z. Zainal, A. J. Ali, A. Kassim and M. Z. Hussein, *Sol. Energy Mater. Sol. Cells*, 2003, **79**, 125–132.
15 R. Indirajith, T. Srinivasan, K. Ramamurthi and R. Gopalakrishnan, *Curr. Appl. Phys.*, 2010, **10**, 1402–1406.
16 D. I. Bletskan, *J. Ovonic Res.*, 2005, **1**, 61–69.
17 G. Domingo, R. S. Itoga and C. R. Kannewurf, *Phys. Rev.*, 1966, **143**, 536–541.
18 A. K. Garg, O. P. Agnihotri, A. K. Jain and R. C. Tyagi, *J. Appl. Phys.*, 1976, **47**, 997–1000.
19 M. M. El-Nahass, *J. Mater. Sci.*, 1992, **27**, 6597–6604.
20 M. Y. Au-Yang and M. L. Cohen, *Phys. Rev.*, 1969, **178**, 1279–1283.
21 P. Pramanik and S. Bhattacharya, *J. Mater. Sci. Lett.*, 1988, **7**, 1305–1306.

22 D. Martínez-Escobar, M. Ramachandran, A. Sánchez-Juárez and J. S. N. Rios, *Thin Solid Films*, 2013, in press.
23 S. Acharya and O. N. Srivastava, *J. Crystal Growth*, 1981, **55**, 395–397.
24 B. Palosz and E. Salje, *J. Appl. Cryst.*, 1989, **22**, 622–623.
25 Z. Zainal, N. Saravanan, K. Anuar, M. Z. Hussein and W. M. M. Yunus, *Mater. Sci. Eng., B*, 2004, **107**, 181–185.
26 N. A. Okereke and A. J. Ekpunobi, *Chalcogenide Lett.*, 2010, **7**, 531–538.
27 Y. Xie, H. Su and Y. Q. B. Li, *Mater. Res. Bull.*, 2000, **35**, 459–464.
28 B. Subramanian, C. Sanjeeviraja and M. Jayachandran, *J. Cryst. Growth*, 2002, **234**, 421–426.
29 N. D. Boscher, C. J. Carmalt, R. G. Palgrave and I. P. Parkin, *Thin Solid Films*, 2008, **516**, 47504757.
30 V. E. Drozd, I. O. Nikiforova, V. B. Bogevolnov, A. M. Yafyasov, E. O. Filatova and D. Papazoglou, *J. Phys. D: Appl. Phys.*, 2009, **42**, 125306.
31 M. Z. Xue, J. Yao, S. C. Cheng and Z. W. Fu, *J. Electrochem. Soc.*, 2006, **153**, 270.
32 R. Teghil, A. Santagata, V. Marotta, S. Orlando, G. Pizzella, A. Giardini-Guidoni and A. Mele, *Appl. Surf. Sci.*, 1995, **90**, 505–514.
33 D. A. Hady, H. Soliman, A. El-Shazly and M. S. Mahmoud, *Vacuum*, 1999, **41**, 375–381.
34 R. Schlaf, N. Armstrong, B. Parkinson, C. Pettenkofer and W. Jaegermann, *Surf. Sci.*, 1997, **385**, 1–14.
35 L. Amalraj, M. Jayachandran and C. Sanjeeviraja, *Mater. Res. Bull.*, 2004, **39**, 2193–2201.
36 M. Popescu, F. Sava, A. Lörinczi, G. Socol, I. Mihăilescu, A. Tomescu and C. Simion, *J. Non-Cryst. Solids*, 2007, **353**, 1865–1869.
37 E. M. G. Albert C. Thompson, David T. Attwood, M. R. Howells, J. B. Kortright, A. L. Robinson, J. H. Underwood, K.-J. Kim, J. Kirz, I. Lindau, P. Pianetta, H. Winick, G. P. Williams and J. H. Scofield, *X-Ray Data Booklet - Center for X-ray Optics and Advanced Light Source - Lawrence Berkeley National Laboratory*, Lawrence Berkeley National Laboratory-University of California-Berkeley, California 94720, USA, 2001.
38 *$SnSe_2$ datasheet number: 01-089-2939; SnSe datasheet number: 04-006-8169*, International centre for diffraction data technical report.
39 B. T. Melekh, N. B. Stepanova, T. A. Fomina and S. A. Semenkovich, *J. Phys. Chem.*, 1971, **45**, 1144–1145.
40 J. Berkowitz and W. A. Chupka, *J. Chem. Phys.*, 1966, **45**, 4289.
41 M. I. Karakhanova, A. S. Pashinkin and A. V. Novoselova, *Inorg. Mater.*, 1967, **3**, 1352–1355.
42 R. Colin and J. Drowart, *Trans. Faraday Soc.*, 1964, **60**, 673–683.
43 H. Wiedemeier and G. Pultz, *Z. anorg. allg. Chem.*, 1983, **499**, 130–144.
44 R. C. Sharma and Y. A. Chang, *Bull. Alloy Phase Diagr.*, 1986, **7**, 68–72.
45 F. K. Lotgering, *J. Inorg. Nucl. Chem.*, 1959, **9**, 113–119.
46 C. Pérez-Vicente and C. Julien, *Mat. Sci. Eng. B*, 1997, **47**, 137–144.
47 V. S. Minaev, S. P. Timoshenkova and V. V. Kalugina, *J. Optoelectron. Adv. M.*, 2005, **7**, 1717–1741.
48 H. R. Chandrasekhar, R. G. Humphreys, U. Zwick and M. Cardona, *Phys. Rev. B*, 1977, **15**, 2177–2183.
49 P. A. Fernandes, P. M. P. Salomé and A. da Cunha, *J. Alloys Compd.*, 2011, **509**, 7600 7606.
50 P. M. P. Salomé, P. A. Fernandes, M. G. Sousa, J. P. Leitao and A. F. Cunha, *J. Phys. Chem.*, submitted article.
51 D. Schroder, *Semiconductor Material and Device Characterization*, Wiley, New York, 2nd edn, 1998.
52 J. Bardeen, F. J. Blatt and L. H. Hall, *Photoconductivity Conference*, Wiley, New York, 1956.
53 R. A. Smith, *Semiconductors*, Cambridge University Press, London, 1959.
54 B. L. Evans and R. A. Hazelwood, *Brit. J. App. Phys.*, 1969, **2**, 1507.
55 K. Liu, H. Liu, J. Wang and L. Feng, *Mater. Lett.*, 2009, **63**, 512–514.